Cholesteric liquid crystal self-organization of gold nanoparticles

Rajaa Bitar, Gonzague Agez, Michel Mitov

Accepted version published in: *Soft Matter*, 2011, **7**, 8198-8206

Cholesteric liquid crystal self-organization of gold nanoparticles

Rajaa Bitar, Gonzague Agez, and Michel Mitov*

Self-organization processes are present in many different inorganic, organic, and biological systems at various length scales and give rise to specific intrinsic physical properties. In the present work, we demonstrate the symbiotic association of gold nanoparticles within a cholesteric (chiral) liquid crystal, and we report the long-range growth of two-dimensional and three-dimensional self-organized arrangements of gold nanoparticles into various cholesteric textures. The structure of these novel nanomaterials is imaged at various scales—from the macroscopic scale of centimeter-size cells to the nanoscale of self-assemblies—and we demonstrate that the nanoparticle pattern depends strongly on film thickness. Furthermore, we investigate how fundamental optical properties such as selective reflection are affected when cholesteric liquid crystals are doped with gold nanoparticles. Potential applications are envisioned in the field of soft nanotechnology and optical materials.

Article history: Received 8th April 2011 / Accepted 13th June 2011 / First published (online) 22th July 2011.

https://doi.org/10.1039/C1SM05628J

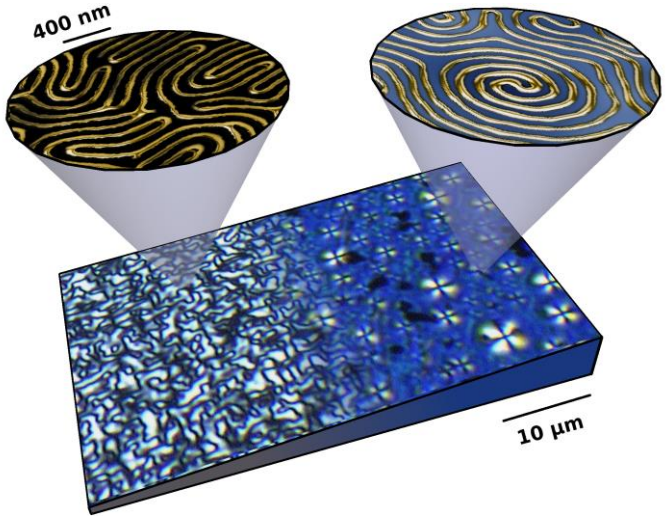

Gold nanoparticles are patterned on demand into various cholesteric textures by playing with the film thickness and the interfacial properties

Centre d'Elaboration de Matériaux et d'Etudes Structurales (CEMES), CNRS, Univ. Toulouse, 29 rue J. Marvig, 31055 Toulouse cedex 4, France. E-mail: mitov@cemes.fr; Fax : +33 5 62 25 79 99 ; Tel : +33 5 62 25 78 61.

Introduction

Motivation for the research

The ability to grow long-range two-dimensional (2D) and three-dimensional (3D) organized arrangements of metallic nanocrystals (NCs) and nanoparticles (NPs) enables the fabrication of materials with novel physical properties [1–3]. To study the effects of mesoscopic ordering on the physical properties, NPs have to be arranged with long-range order into larger organized structures. For example, the photoluminescence properties of CdSe NPs depend on their order in a 3D assembly [4], and vibrational coherence in Raman scattering is observed when silver NCs are ordered in a face-centered-cubic supracrystal [5]. The aim of self-organizing NPs into anisotropic networks is motivated by the benefits expected for fabricating electronic, optical, and electro-optical devices and sensors.

A grand challenge is thus to assemble and position NPs in desired locations to build larger-scale nanostructured materials. A self-assembly method is highly desirable because of its simplicity and compatibility with multicomponent integration processes, and research into efficient self-assembly protocols to manipulate nanoscale building blocks into functional nanomaterials has created enormous excitement in the field of liquid-crystal (LC) research [6, 7]. LCs are excellent candidates for matrix-guided self-assembly because the LC state combines order and mobility at the molecular (nanoscale) level and because the coupling of particles with the orientational order of the LC phase may give rise to hybrid materials with novel properties, motivating the development of new optical elements, photonic structures, electronic devices, or metamaterials.

Among metallic NPs, gold NPs (GNPs) are the most frequently studied because the related stabilizing techniques are likely the best understood [1, 2]. GNPs present fascinating properties such as their capacity to be organized into multiple and versatile patterns, their size-related electronic, magnetic, and optical properties, and their applications in catalysis and biology. GNPs are often cited as key materials and building blocks for the 21st century in the context of emerging nanoscience and nanotechnology (*i.e.*, the bottom-up approach).

The present work focuses on the dispersion of GNPs in a thermotropic cholesteric LC (CLC). The helical structure of a CLC comes from the molecular chirality of constitutive molecules (in whole or in part). The cholesteric structure is omnipresent in living matter [8–14] and concerns many applications in optics because of its property of selective light

reflection [15–17]. Our choice of using a CLC framework to organize GNPs is motivated by the huge variety of chiral textures that are available (oily streaks, fingerprints and fingering, grids, fan-shaped focal conics, Grandjean steps, etc.) [18] and the opportunity to investigate the unique optical properties of CLCs (selective light reflection, polarization-selectivity rule, strong optical rotatory power) when it is doped with GNPs.

State of the art and present objectives

The majority of studies involving LCs as templates for NP patterning use lyotropic LC phases—scarcely thermotropic phases—and deals with the nematic (achiral) phase. In some studies, GNPs were dispersed into nematic LCs [19–22], in others the mesogens were directly grafted on the GNPs [23–26] or the GNPs were synthesized *in situ* (*i.e.*, in the LC) [27]. However, investigations of GNPs dispersed into a chiral—and *a fortiori* cholesteric—LC phases are very scarce. It has been reported that temperature range of (chiral) blue phases rises from 0.5 to 5.0°C upon doping the LC with GNPs [28]. The NPs aggregate in the lattice of disclination lines, which reduces the free-energy penalty for disclination lines. Theoretical arguments also support this interpretation [29, 30, 31].

The present study is based on our work on the self-assembly of platinum (Pt) NPs in a CLC [32]. The material consisted of an open film directly coated on a copper grid for transmission electron microscopy (TEM). The interfaces were between air and a polymer film (parlodion) coated with carbon and deposited on the grid. The main conclusions of this work are: (i) the long-range self-assembly of NPs as a stripe—or fingerprint—texture was demonstrated, the periodicity of NP ribbons is directly related to the helix periodicity and indirectly to the molecular chirality, and a stripe texture with a larger periodicity than the pristine texture was fabricated; (ii) NPs were rejected at the interfaces, and the self-assembly of NPs into fingerprint patterns occurred only close to the air interface where the boundary conditions are homeotropic [33–35]; and (iii) the NPs localize in regions that exhibit strong distortions in the molecular-director distribution [33–35].

The objectives of the present study are: (i) to target the self-assembly of gold NPs into various CLC patterns (this aim is of paramount importance due to the potential optical properties of GNPs in comparison with those of Pt NPs); (ii) to generalize the fabrication procedure so that nanopatterned films may be fabricated on more than just a TEM grid; (iii) to better understand the driving parameters that lead to novel and peculiar patterns (*i.e.*, much

more than parallel stripes); (iv) to directly image the GNP patterns at the meso- and nanoscale by scanning electron microscopy (SEM), TEM, and atomic force microscopy (AFM); and, finally, (iv) to investigate the reflection properties of the nanomaterial versus those of undoped CLC film; the impact of ordered GNP networks on the reflectivity of chiral liquid-crystalline hosts has not been addressed in literature. All these objectives correspond to open questions in the field of soft nanocomposites.

Materials and methods

Materials

CLC oligomers from Wacker Chemie GmbH were used (Fig. 1a). The molecule is a siloxane cyclic chain with two types of side chains attached via spacers: an achiral mesogen and a (chiral) cholesterol-bearing mesogen [36, 37]. When coated on a glass or plastic substrate, the compound exhibits typical iridescent colors that range from blue to red upon tuning the molar percentage of chiral mesogens in the oligomer molecule. This molar percentage can vary from 31% to 50%. These materials have given rise to rich and various studies, including basic investigations of their reflection properties [38], the fabrication of optical notch filters [39], the first quenching of blue phases [40, 41], the measurements of the optical activity of blue phases [42], the first low-frequency mechanical relaxation measurements of molecular motions near the glass-transition temperature [43], evidence of asymmetry phenomena in transmission profiles [44], fabrication of broadband reflectors [45–48], Raman-spectrometry mapping of a pitch-gradient structure [49], color gamut of planar films and flakes by colorimetry [50, 51], the electro-optical behavior of flakes [52], mechano-optical effects [53], lasing from dye-doped materials [54], or interface-induced color effects [55].

We have blended so-called silicon blue (SB) and silicon red (SR) compounds at 40:60 wt.% to tune the mean position of the reflection band to the middle of the visible spectrum (*i.e.*, 560 nm). The cholesteric phase appears between 180 and 210 °C (clearing temperature range) and 40 to 50 °C (glass-transition temperature range). A thin film with cholesteric organization and the related reflection properties can easily be quenched below the glass-transition temperature, in which case it becomes a solid film that can be handled at room temperature. These characteristics are of paramount important to reach the objectives of the present study.

Spherical GNPs functionalized with octanethiol from Sigma Aldrich (reference 660426) were used (Fig. 1b). The average GNP diameter was 3 nm and the particles were suspended in toluene, which is also a very good solvent for the oligomers.

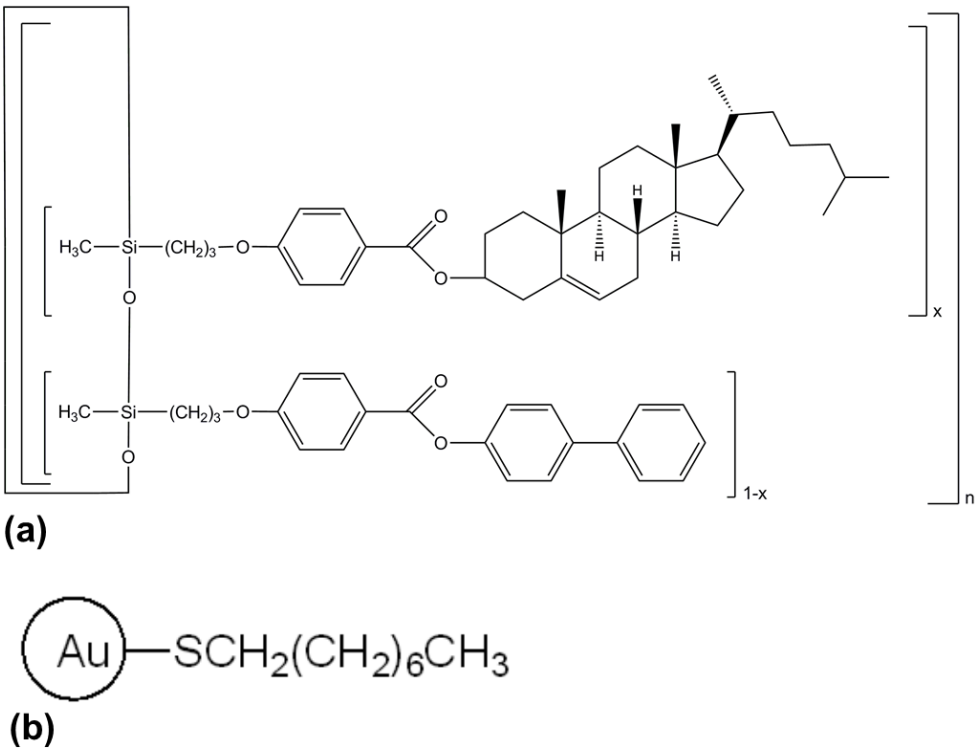

Fig. 1. Chemical structure of materials. (a) Cholesteric liquid crystal oligomers (image courtesy of Dr. E. Hanelt). The quantity *x* is the molar fraction of the chiral mesogen and *n* represents the ring size of the siloxane backbone. (b) Gold nanoparticle functionalized with octanethiol.

Methods

Optical textures

We investigated the optical texture of the films in transmission and reflection modes by using a polarizing microscope (AX70 from Olympus). The images were obtained by using a TRI CCD F22GV camera from Hitachi with a numerical resolution of 0.13 μm/pixel.

Scanning electron microscopy imaging

We used a JSM-6490 SEM (Figs. 3 and 4) and a JSM-6700F SEM-FEG (Fig. 5) from JEOL. Samples were coated with a chromium film (Figs. 3 and 4, thickness was 2 nm) or platinum (Fig. 5, thickness was 1 nm) to create a conductive surface and fixed on the support with a carbon-coated adhesive. Investigations were performed in backscattered-electron mode, which provides a composition contrast that distinguishes the gold from the LC surrounding.

Preparation of samples for transmission electron microscopy

A small piece of film was embedded in an epoxy resin and the inclusion was then cured at 40 °C. Thin slices of material were obtained with an ultramicrotome (UltraCut S from Reichert) by using a diamond knife at ambient temperature. The material was cut perpendicularly to the film surface (cross sections) and 80-nm-thick slices were directly retrieved on carbon-coated grids.

Transmission electron microscopy conditions

Investigations using high-angle annular dark-field-scanning transmission electron microscopy (HAADF–STEM) were performed in the FEI Titan transmission electron microscope equipped with a probe corrector and operating at 300 kV. The aperture of the condenser lens was 100 microns. An ADF image formed at very high angle is highly sensitive to variations in the atomic number *Z* of atoms in the sample (*Z*-contrast images).

Atomic force microscopy imaging

AFM measurements were performed at room temperature and under ambient conditions using a Veeco Dimension Icon AFM system controlled by a NanoScope V controller. The images were obtained in tapping mode.

Image analysis

The spatial periodicity of the periodic structures (Fig. 3, Fig. 4 C and D) is measured by using

a two-dimensional FFT (Fast Fourier Transform). The error range is the FWHM (Full Width of Half Maximum) of the spatial peak frequency and provides information on the dispersion of the periodicity in the whole texture.

Transmittance properties

The film transmittance was investigated at room temperature and at normal incidence by using a Cary 5000 spectrometer from Varian and an Ocean Optics USB4000 fiber optic spectrometer with an external halogen light source HL-2000 from Mikropack. The incident light was unpolarized.

Determination of film thickness

The film thickness was determined by the interference method using a spectrophotometer. The method is based on the wavelength dependence of the transmission interference pattern, which is due to the internal reflection between the two inner surfaces of the cell substrates [55].

Results and discussion

CLC-GNPs hybrid-film fabrication method

The steps for fabricating hybrid films are as follows: (1) The oligomer is blended with GNPs and toluene. The quantities are chosen to target a final GNP concentration equal to 1 wt.% after evaporation of the toluene. (2) The solution is put in a vial that is sonicated in water for 1 h. (3) The solution is poured into a glass watch and kept at 140 °C for 5 min to allow the toluene to evaporate. (4) The mixture is introduced at 140 °C between glass plates whose the variable gap is controlled with Mylar spacers. No peculiar surface treatment or alignment layers are used on the glass surfaces. (5) The cell is quenched by putting it swiftly on a metallic substrate at room temperature (RT). Consequently, the viscous film changes into a solid glassy film. (6) The cell is kept at a low temperature (2 °C) to facilitate the clean removal of the cover glass and to obtain a smooth interface. This process yields an exposed film ready to be annealed. (7) The film is annealed at 140 °C for 18 h. (8) The sample is

finally quenched by putting it swiftly onto a metallic substrate at RT. The preferential molecular orientation is planar on the glass substrate and homeotropic (perpendicular) at the air-material interface.

Investigation of textures

The undoped open film presents a mosaic of adjacent cells (Fig. 2a).

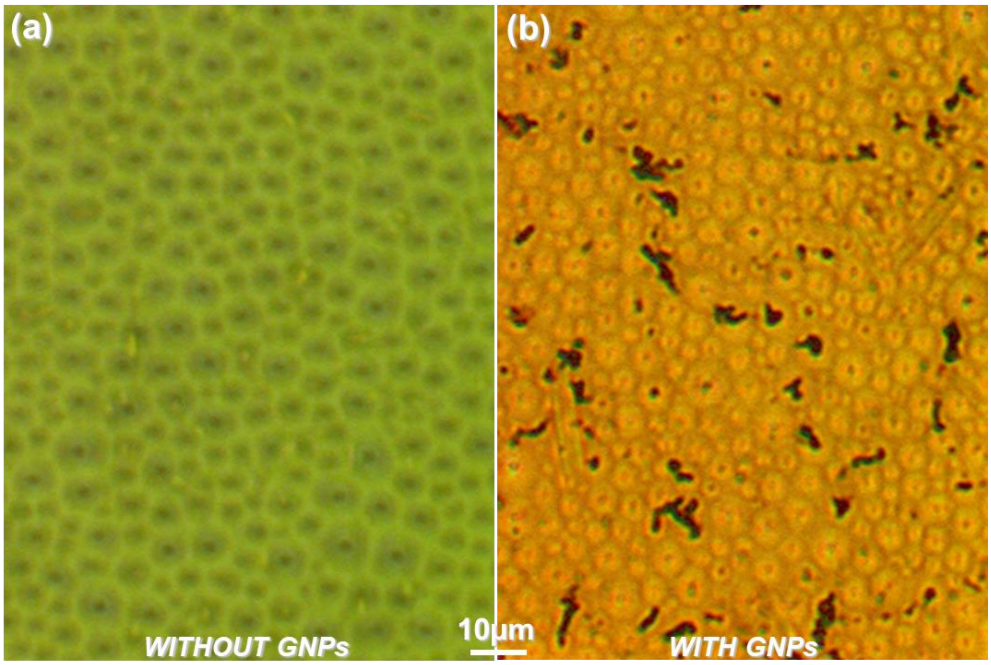

Fig. 2. Optical textures of cholesteric films **(a)** without and **(b)** with gold nanoparticles. Film thickness was 13 μm. Data acquired in transmission mode and incident light was unpolarized.

Each cell appears as a dark greenish polygon with a central black spot and is surrounded by a bright green region. This is referred to as the polygonal texture [57, 58]. We have previously investigated in detail the 3D structure of the polygonal texture by combining different and complementary imaging techniques and have also investigated the related optical properties [55]. AFM images of the free surface shows that the polygons are convex cones 20 to 100 nm tall. Close to the free surface, the twisted structure cannot readily adapt to the anchoring conditions. One solution to this boundary problem is the creation of a series of alternating disclination lines at the free surface. The equilibrium relief results from competition between surface energy and bulk free energy. The energy is lowered by transforming the free surface into a cone, thus reducing the bulk distortion energy at the expense of surface energy. We

have also shown that the wavelength reflected from the cholesteric film may be selected simply by varying the annealing time. This effect was demonstrated by TEM cross-sectional investigations that showed that color changes are due to controlled changes of the orientation of the helix axis with respect to the air-material interface.

The polygonal texture is preserved after doping the CLC with GNPs (Fig. 2b). GNP aggregates appear in black in Fig. 2b. These aggregates are present immediately after the solvent evaporates (*i.e.*, after the end of step 3 of the fabrication procedure), so these aggregates are not the consequence of the time-driven self-assembly process. The aggregation phenomenon might be reduced by increasing the sonication and annealing times. The crucial thing to determine is if GNPs are present in the texture apart from the aggregates and, if so, what their mutual organization is. To address this point, we used SEM in backscattered electron mode, and the results are shown in Fig. 3, where the gold appears in white and light grey. Originally, the GNPs exhibit regular fingerprint-type cholesteric textures with double-spiral patterns. The helical axis is everywhere perpendicular to the lines. The spiral pitch (*i.e.*, the distance between two identical lines) is equal to 340 ± 60 nm. This periodicity is related to the half-pitch of the cholesteric structure (the cholesteric structure looks the same physically and has the same dielectric properties after a 180° rotation), but is greater than the half-pitch of the undoped cholesteric structure, which is 180 ± 10 nm (see Supplementary Information of [55]). The present pattern formation is thus rigorously a self-assembly mechanism; it is not a well-known texture-decoration process, when an additive precipitates along the disclination lines at the free surface of a CLC as crystallites [59] or droplets [60], with a size in the micrometer range. Every double-spiral corresponds to a polygonal cell, as seen in Fig. 2b. The darker spot that appears in Fig. 3 in the background associated with a double-spiral corresponds to the relief of the convex cone.

We show below that the GNP pattern fundamentally depends on the film thickness.

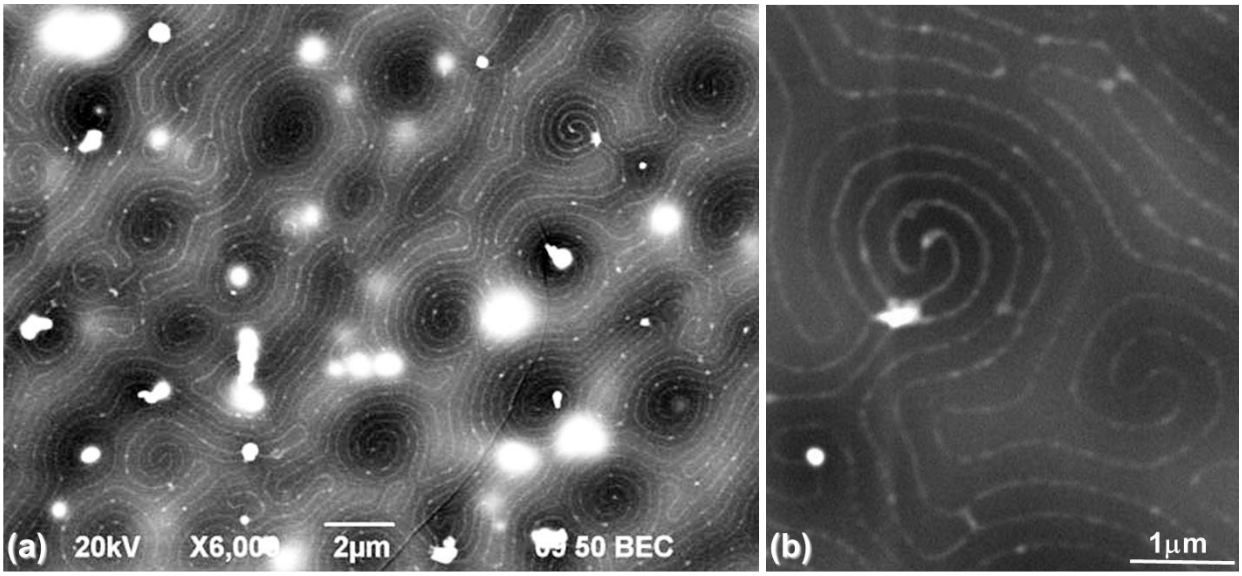

Fig. 3. (a) Network of double spiral cholesteric patterns of gold nanoparticles. **(b)** Magmified view of a pair of double spirals. SEM (backscattered electron mode). Gold appears everywhere in white and light grey. Film thickness was 13 µm.

Crucial role of film thickness in determining GNP patterns

For very thin films (<2 µm), the GNP patterns that appear upon increasing the film thickness are (Fig. 4):

(A) very short lines associated with the nucleation of GNP ribbons. The film thickness impacts the helical twist in a direction perpendicular to the film surface—a thinner film hinders the development of the twist. The helical structure has to adapt to this situation of geometrical frustration. Because of the symbiotic association of GNPs with the (partially unwound) CLC structure, only ribbon nuclei are thus visible for the thinnest films.

(B) longer lines partially connected together. Upon increasing the thickness, the frustration relaxes and longer GNP chains may grow.

(C) a very regular network of periodic lines called the fingerprint texture. The periodicity is equal to 210 ± 20 nm. Only above a film-thickness threshold may a network of GNP chains propagate. Our earlier investigations [32–35] addressed the case of open films directly coated on TEM grids. In that case, observations were only possible in the grid holes where the film thickness was sufficiently thin to be sufficiently transparent to the electron beam. For this reason, our previous description deals only with isolated NP fingers and fingerprint patterns.

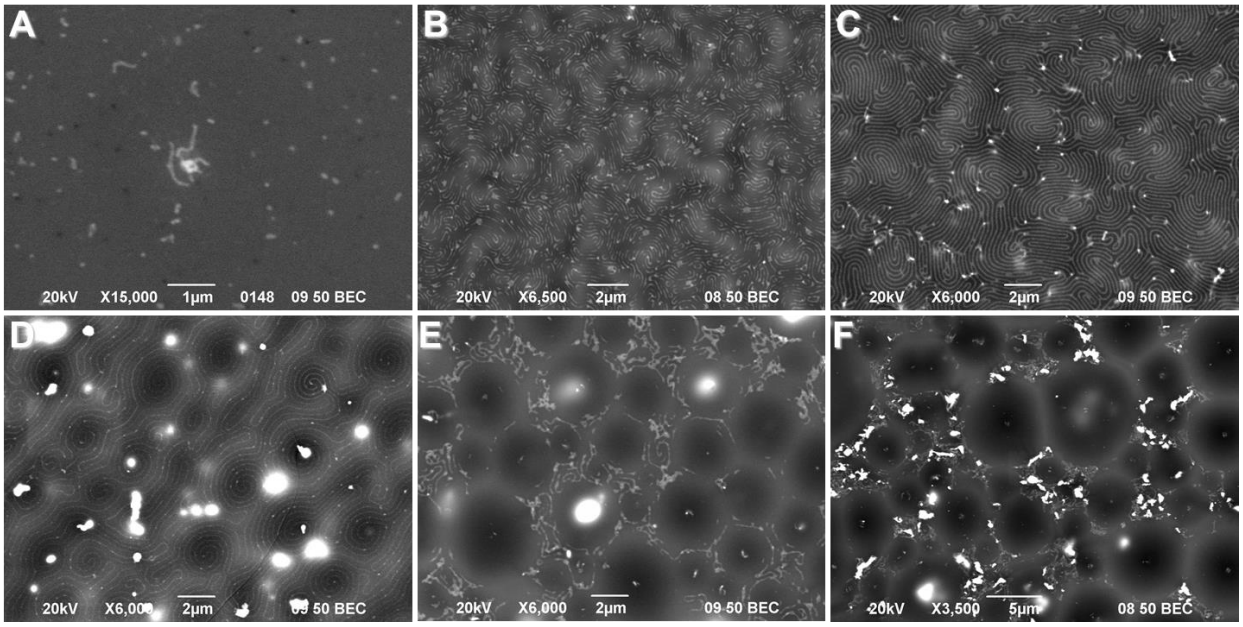

Fig. 4. Sequence of cholesteric patterns of gold nanoparticles when the thickness increases (SEM, backscattered electrons mode). Two thickness regimes are described. Thickness < 2 µm: **(A)** nuclei, **(B)** fingers, **(C)** fingerprint texture. Thickness > 2 µm: **(D)** double-spiral network (thickness range was 2 to 12 µm), **(E)** targets (thickness range was 12 to 25 µm), **(F)** aggregates (thickness > 25 µm).

For films thicker than 2 µm, the GNP patterns that appear upon increasing the thickness are:

(D) in the 2 to 12 µm range [61], GNPs self-assemble into a network of double spirals. The width of the spiral arms depends on the NP density and, as a consequence, increases with film thickness. Figure 5 shows a magnification of a gold spiral observed in a film made as thin as possible. We observe a very thin spiral arm made from only a few GNPs.

(E) in the 12 to 25 µm range, GNPs self-assemble as targets; namely, a ring with a spot in the center (like a corral self-assembly). Additionally, GNP aggregates are visible. These aggregates are the consequence of the self-assembly mechanism for this peculiar thickness range; they do not have the same status as the aggregates observed in Figs. 2b and 3.

(F) finally, for films thicker than 25 µm, large-size aggregates form the dominant patterns. When the thickness increases past a threshold, more and more NPs are available to migrate close to the air interface and a saturation phenomenon appears. Anisotropic self-assembly of GNPs in close relation with the mesomorphic texture becomes difficult,

and symbiotic cholesteric patterns of GNPs are ruined by the presence of too many GNPs.

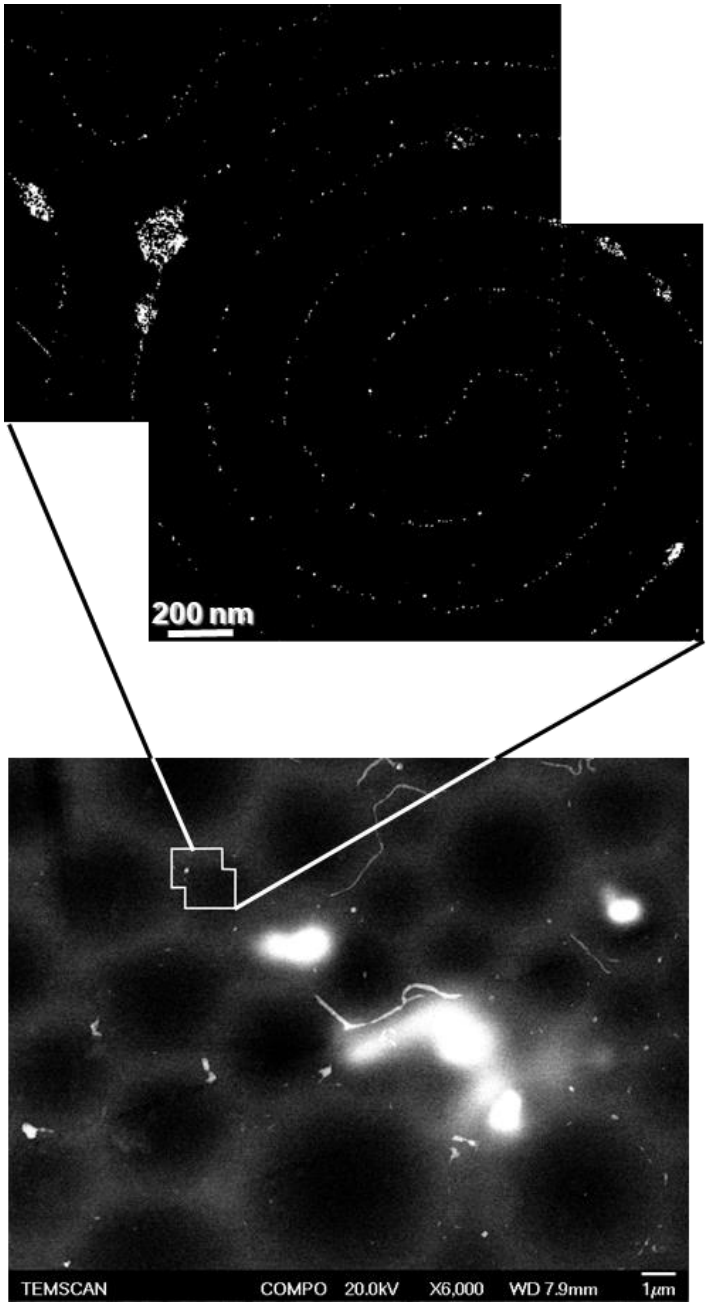

Fig. 5. Magnified view of a double spiral for film as thin as possible—close to 2 μm (SEM, backscattered electrons mode). This situation corresponds to a spiral with a very thin arm made with a significantly reduced number of gold nanoparticles.

Figure 6 summarizes the evolution of GNP patterns for the various thickness ranges.

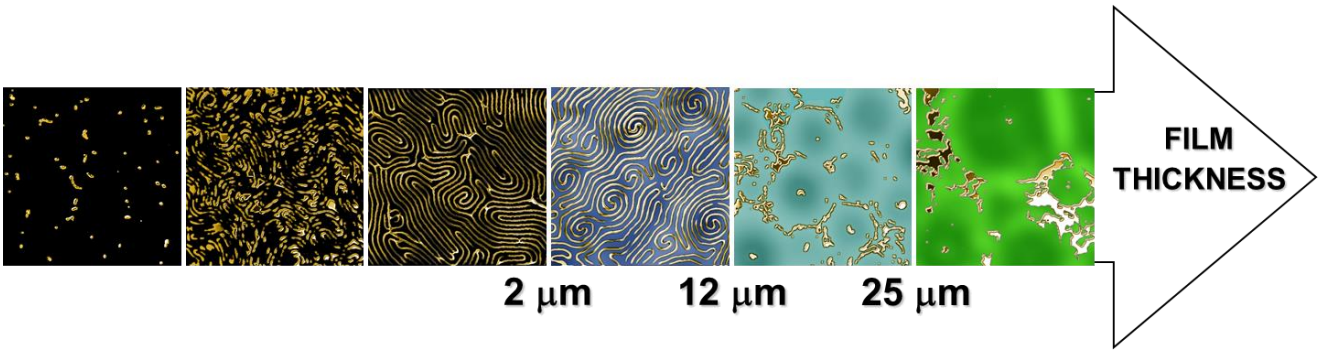

Fig. 6. Scheme to summarize dependence of gold pattern on thickness.

That the quenched films are solid state provides a unique opportunity to image their cross-sectional structure by TEM. The image in Fig. 7 shows parallel dark and bright lines that are perpendicular to the air-material interface for GNPs dispersed in the SB oligomer. The origin of the TEM line contrast in the oligomers has been discussed in Refs. [62–66]. Figure 7 shows, for the first time, the correlation between the fingerprint texture of the (GNP-free) bulky CLC and the sites of GNPs close to the free surface. These latter appear as regularly spaced GNP groups because the periodic ribbons are cut orthogonal to their long axis. In the fingerprint texture of the CLC alone, every group is localized at the extremity of a dark line. By analogy with the TEM investigations of GNP patterns in the plane of the film when it is directly deposited on a grid, we conclude that the GNPs preferentially fit into the regions of the film surface where LC molecules are preferentially oriented parallel to the film plane (see the insert in Fig. 7).

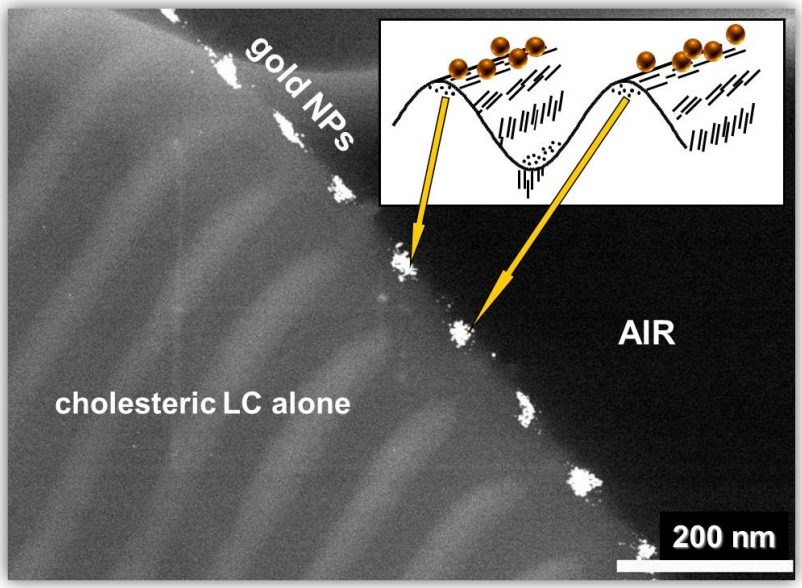

Fig. 7. Cross-sectional view of cholesteric film doped with gold nanoparticles showing the correspondence between fingerprint texture of a pure liquid crystal and localization of nanoparticles at the free surface of the film after annealing (18 h). HAADF-STEM. Insert: scheme to show the relation between the position of nanoparticles at the free surface and the orientation of rod-like liquid crystalline molecules at the immediate surrounding.

Additionally, AFM investigations (Fig. 8) give hints of the 3D nature of the long-range organization of GNPs and offer information about the height of the GNP chains that emerge from the film surface (typically in the 3 to 10 nm range).

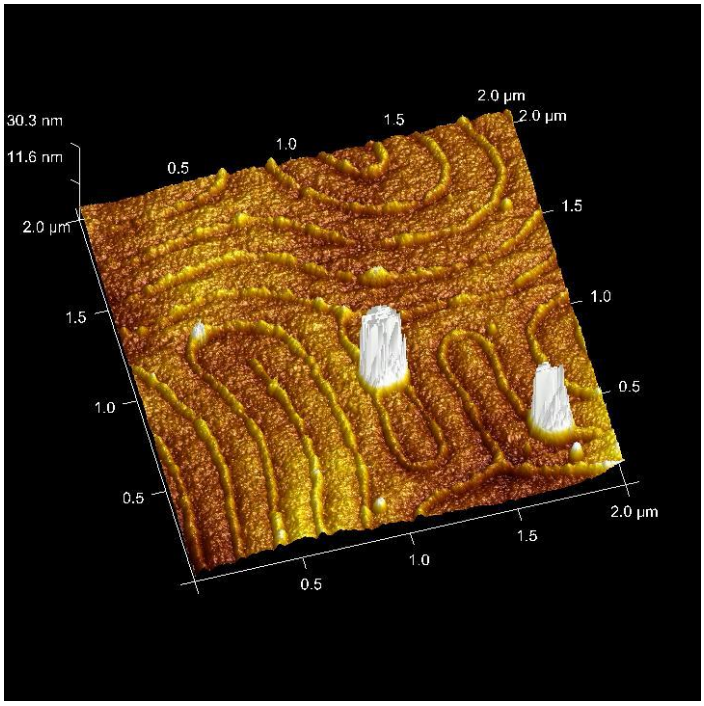

Fig. 8. AFM image of gold fingerprint texture. The pair of white domes are aggregates as seen in black by optical microscopy (Fig. 2b) or in white by SEM (Fig. 4c).

To summarize, we find that, although self-assembly occurs at the free surface, the film thickness is a crucial parameter in determining the particular GNP pattern that forms and in avoiding the isotropic aggregation of NPs, such as random clusters, that forms with time (up to 18 h in the present work). To reach these objectives, the correct thickness range must be chosen. This insight is important because the question of NP aggregation in suspension in a LC, which leads to unstable films, is a topical subject in the field of LC colloids because it can restrict scientific investigations as well as technological applications.

Reflection band

The central reflection wavelength λ_0 of a CLC structure is directly related to the helical pitch p (structural periodicity that represents a rotation of 360° in the orientation of the rod-like molecules) by Bragg's law: $\lambda_0 = np\cos\theta$, where n is the average refractive index and θ is the angle between the direction of light propagation and the helix axis [67–69]. As shown in Fig. 9a, the Bragg band is centered at 560 nm and is not significantly modified by the presence of GNPs before annealing. After 18 h of annealing, λ_0 shifts from 560 to 450 nm for the pure LC film (Fig. 9b). We have reported and discussed this phenomenon in a previous publication

[55], where we concluded that (i) this blue shift is due to changes in the helix-axis orientation with respect to the air-material interface, and this orientation propagates into the film volume with increasing annealing time, and (ii) the transmittance losses (clearly visible in Fig. 9b) are due to a strong off-axis reflection (because the characterization was made at normal incidence, light reflected at oblique incidence was not collected) and to light scattering induced by the cell boundaries (*i.e.*, cones) in the polygonal texture (Fig. 2), which create defects.

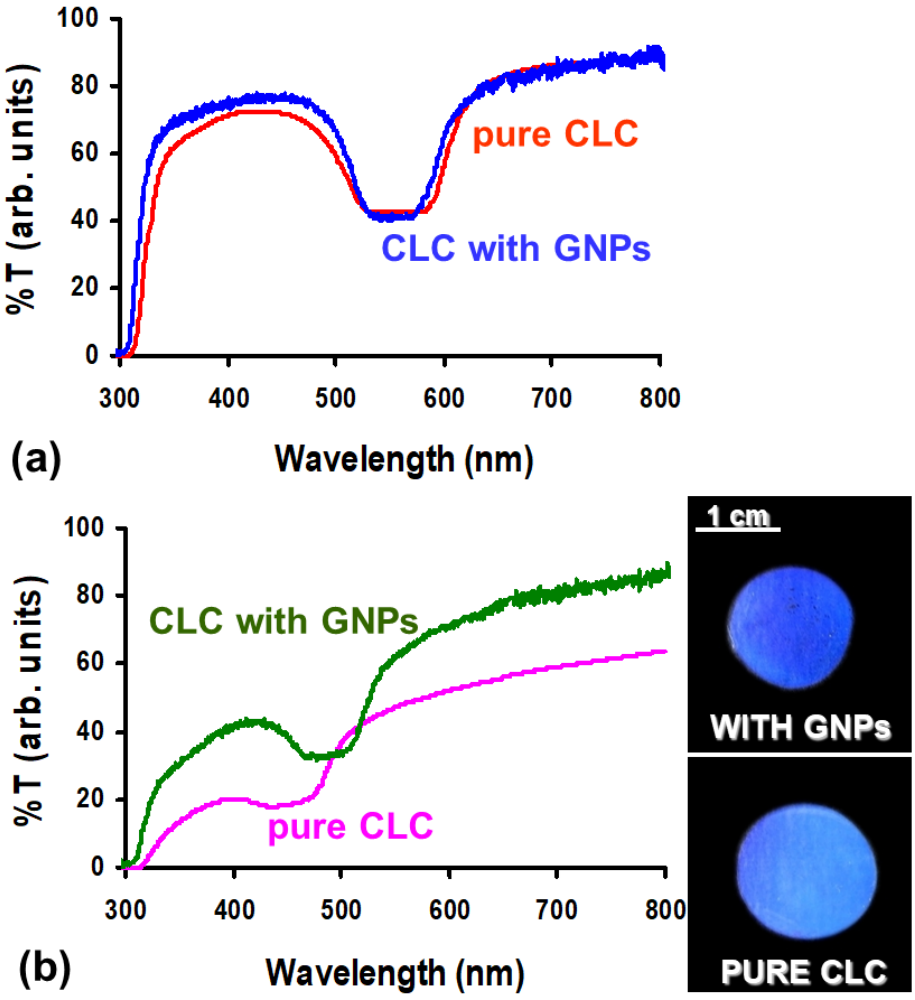

Fig. 9. Transmittance spectra of cholesteric films with and without gold nanoparticles **(a)** before and **(b)** after annealing (18 h). Inset shows images of experimental cells after annealing with and without gold nanoparticles. Film thickness was 13 μm.

When the behavior of the hybrid film is compared to that of the pure film (Fig. 9b), it is apparent that the blue-shift is weakened in presence of GNPs. The central wavelength λ_0 shifts

from 560 nm to only 490 nm (as opposed to 450 nm for the pure film), and this shift lag is systematically reproducible. The GNPs change the anchoring properties of the open film at the air-material interface at both the nano- and mesoscale. At the nanoscale, GNPs in the size regime between 1 and 5 nm and coated with thiolates have been shown to promote homeotropic anchoring of LC molecules to the particle surface and are capable of forming topological defects generating elastic forces in CLCs that lead to the formation of chain-like particle aggregates [20].

At the microscale, we believe that the optical texture is modified because the propagation of distortions from the free interface is modified by the presence of particles. We know that the anchoring properties determine the optical properties of the pure film (*i.e.*, the characteristics of the blue-shift) for increasing annealing time [55]. Therefore, the anchoring conditions at the beginning of the annealing process are essential because they determine which structure appears as the annealing proceeds.

The presence of a network of self-organized GNPs at the interface makes the interface stiffer and delays the propagation of distortions, which explains the shift lag induced by the presence of GNPs. Therefore, the color of the entire cholesteric film induced by the presence of GNPs appears to be a consequence of changes in the nature of the anchoring rather than a consequence of the modification of the helical periodicity in the bulk of the film.

Macroscopically, both experimental cells exhibit blue reflections (see inserts of Fig. 9b), but the pure cell exhibits a bluish milky state, which is a consequence of additional light-scattering properties that are noticeably attenuated when the cell is doped with GNPs.

We also investigated the dependence of the Bragg band on film thickness after annealing (Fig. 10). The right edge of the Bragg band (*i.e.*, the maximum wavelength of the band-gap plateau, see insert of Fig. 10) as a function of thickness is presented, along with the related textures in both transmission and reflection modes. Although focal conic cholesteric textures are observed when the thickness is less than 2 μm (textures B and C), no significant reflected light intensity is detected by spectrophotometry. All samples between 2 and 30 μm thick (textures D to G) are light-reflecting materials and the maximum wavelength increases with film thickness.

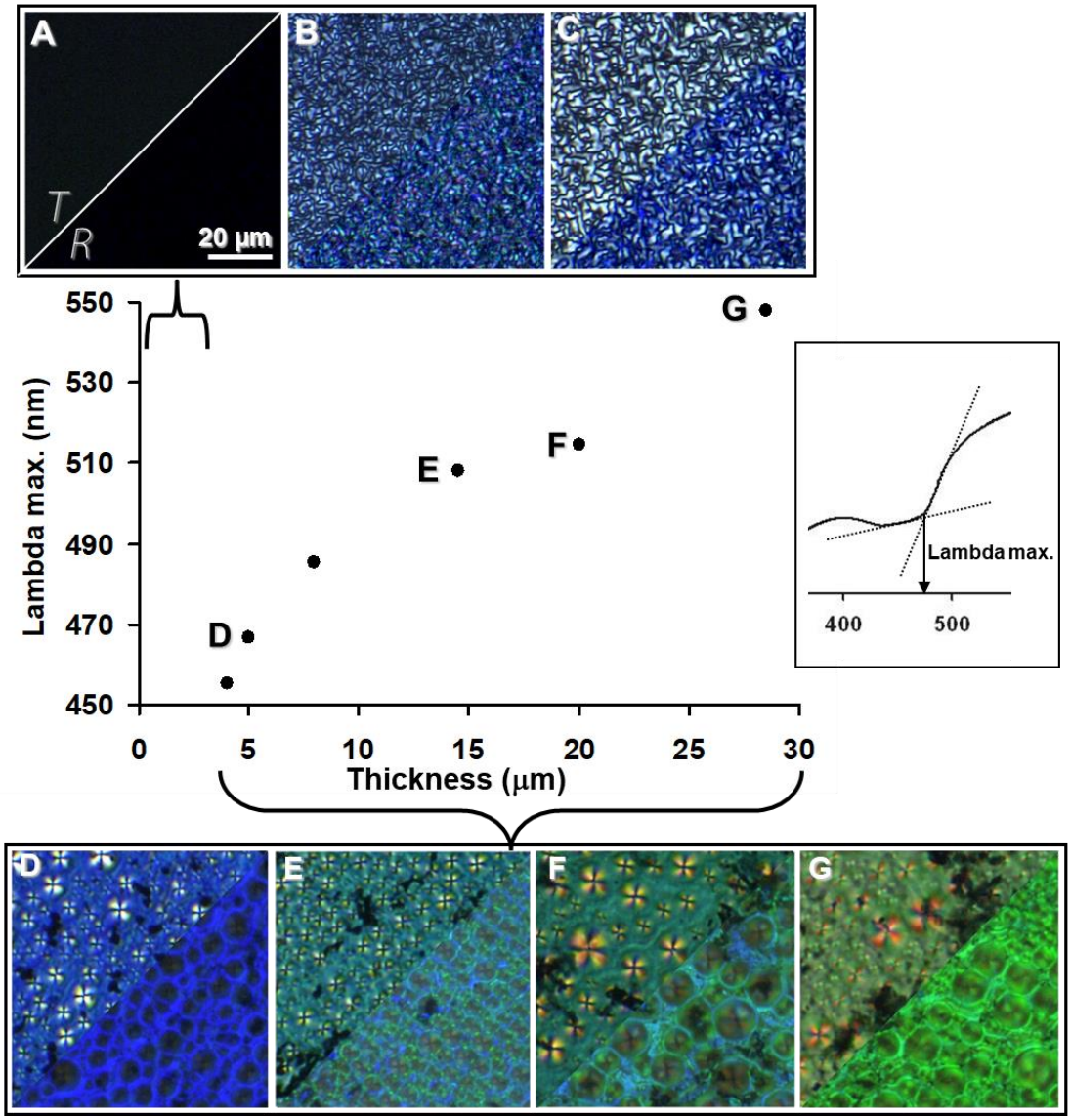

Fig. 10. Reflection wavelength as function of film thickness (unpolarized incident light). The wavelength (lambda max.) is the right-edge value of the band-gap plateau (as shown in the inserted drawing). Inset shows optical textures (crossed polarizers) in transmission (*T*) and reflection (*R*) modes for increasing film thickness. Images A, B, and C (*resp.* D to G) correspond to thicknesses < 2 µm (*resp.* between 5 and 30 µm).

This result means that the blue-shift phenomenon vanishes when the thickness increases. This behavior can be understood through an analogy with the behavior of undoped CLCs [55]: The blue-shift is related to the propagation of distortions from the air-material interface into the film volume, and these distortions induce a distribution in the orientation of the helical axis in the film volume. For a single annealing time (18 h), it is expected that the distortions propagate entirely across the thinner films but only across a fraction of the thicker films (and

this behavior is even made more dramatic by the presence of GNPs that induce a shift lag, as discussed above). For these reasons, thicker films reflect preferably in the green (*i.e.*, the pristine color of the film, before the distortions modify the Bragg response), as opposed to the blue.

The impact of NPs on the reflection properties of a thermotropic CLC confined in a glass sandwich-cell has been addressed in a recent publication [70]. The research used silica NPs with an average diameter of 40 nm and a concentration of 3.4 wt.%. The results show that NPs behave like impurities that disrupt the helical structure and that reflectivity is inhibited. The authors claim that NPs at surfaces of cell substrates disrupt the ability of the sample to conform to the rubbed polyimide layers, and the planar texture that would give rise to Bragg reflections is consequently not promoted. Thus, they conclude that 40-nm-diameter particles cannot be accommodated within the CLC phase without substantial distortion. In addition, they report a low reflectivity (15%). For comparison, the reflectivity of pure CLCs is 30% when treated with toluene and 50%–60% when untreated. This tendency is contrary to what we observe in our system, where CLCs doped with GNPs exhibit less scattering than CLCs alone. Our experiments, which use smaller size NPs, provide materials that maintain a helical structure with clear-cut reflection properties and a proper behavior (*i.e.*, shift lag) in comparison with that of the undoped material.

A quantitative analysis of reflected intensity to compare with the quantities given in Ref. [70] is not relevant because of the very different cell geometries. Indeed, the cell in Ref. [70] corresponds to a confined glass cell with planar anchoring at both interfaces, whereas our cell is an open film with planar anchoring close to the solid substrate and homeotropic anchoring close to the interface with air, which leads to significant off-axis reflection. Thus, for the cell used in the present work, only part of the reflected flux is concerned in characterizing the transmittance properties at normal incidence.

Conclusions

We dispersed GNPs in a CLC and investigated the structural and optical properties of the resulting materials. Data on these topics were missing in the literature. The materials demonstrate a symbiotic association of GNPs with a chiral texture and the nanopatterned materials may be fabricated with high reproducibility and on large surfaces (several mm^2). We have succeeded in coating the open film onto a huge variety of substrates: a TEM copper

grid coated with a polymer film, a glass plate, a plastic foil, and even the surface of water. In the latter case, the GNPs embedded in the CLC thin film can be transferred from the floating film onto a choice of substrates in a simple dip-coating fashion.

Because the films were in the solid state, we used TEM and SEM to investigate the LC texture as well as the NP patterns. The patterning occurs close to the air-material interface in regions where distortions in the molecular-director distribution are strongest. The line periodicity—for parallel-line patterns as well as for double-spiral networks—may be directly tuned via the cholesteric pitch.

Furthermore, NP aggregation with time may be limited by choosing the right film-thickness range. Controlling the film thickness is also a manner in which to select the targeted GNP pattern; for example, parallel lines of tunable length, spirals with tunable arm width, and targets. The film thickness also affects the expansion of the cholesteric twist in the third direction, the type of fingerprint texture obtained (isolated fingers, fingerprints, spiral networks), and the quantity of NPs available to migrate towards the air interface.

We also describe the impact of GNPs on the reflection properties of CLC materials as a function of film thickness. GNPs induce a lag in the blue-shift that comes from distortions in the helical-axis-orientation distribution, because GNPs change the nature of the air-material interface.

The demonstration herein of the self-organization of NPs into versatile patterns induced by cholesteric structure is seen as a starting point toward an inexpensive bottom-up technique for on-demand selective positioning and patterning of NPs over large areas.

Acknowledgments

This work was supported by the Agence Nationale de la Recherche (ANR) under grant number 07-NANO-032. We thank: Dr. E. Hanelt from Wacker Chemie GmbH (Munich, Germany) for providing us with oligomers and constant support, Mr. S. Leblond du Plouy (Univ. Paul-Sabatier, Toulouse, France) for his technical assistance with SEM-FEG, Mr. C. Bourgerette (CEMES–CNRS) for his technical assistance with ultramicrotomy, Dr. F. Houdellier (CEMES–CNRS) for STEM observations performed at Laboratorio de Microscopías Avanzadas (University of Zaragoza, Spain), and Mr. M. Febvre (from Bruker AXS, Palaiseau, France) for the AFM investigations.

References and notes

1 M.-C. Daniel and D. Astruc, *Chem. Rev*., 2004, **104**, 293–346.

2 V. Sharma, K. Park and M. Srinivasarao, *Mat. Sci. and Eng. R*, 2009, **65**, 1–38.

3 I. Lisiecki and M.-P. Pileni, *C. R. Chimie*, 2009, **12**, 235–246.

4 N. Zaitseva, Z. Rong Dai, F. R. Leon and D. Krol, *J. Am. Chem. Soc*., 2005, **127**, 10221–10226.

5 A. Courty, A. Mermet, P. A. Albouy, E. Duval and M. P. Pileni, *Nature Mater*., 2005, **4**, 395–398.

6 J. W. Goodby, I. M. Saez, S. J. Cowling, V. Görtz, M. Draper, A. W. Hall, S. Sia, G. Cosquer, S.-E. Lee and E. P. Raynes, *Angew. Chem. Int. Ed*., 2008, **47**, 2754–2787.

7 H. K. Bisoyi and S. Kumar, *Chem. Soc. Rev*., 2011, **40**, 306–319.

8 A. C. Neville, in *Biology of Fibrous Composites*, Cambridge University Press, 1993.

9 M. M. Giraud-Guille, *Current Opinion in Solid State & Mat. Sci*., 1998, **3**, 221–227.

10 S. Berthier, in *Iridescences—The Physical Colors of Insects*, Springer-Verlag, New York, 2006.

11 Y. Bouligand, *C. R. Chimie*, 2008, **11**, 281–296.

12 M. M. Giraud-Guille, G. Mosser and E. Belamie, *Current Opinion in Colloid & Interface Sci*., 2008, **13**, 303–313.

13 A. D. Rey, *Soft Matter*, 2010, **6**, 3402–3429.

14 I. W. Hamley, *Soft Matter*, 2010, **6,** 1863–1871.

15 *Chirality in Liquid Crystals*, ed. H.-S. Kitzerow and C. Bahr, Springer-Verlag, New York, 2001.

16 *Reflective Liquid Crystal Displays*, ed. S.-T. Wu, D.-K. Yang, Wiley-VCH, Chichester, 2001.

17 *Liquid Crystals—Frontiers in Biomedical Applications*, ed. S. J. Woltman, G. D. Jay and G. P. Crawford, World Scientific, Singapore, 2007.

18 I. Dierking, in *Textures of Liquid Crystals*, Wiley-VCH, Wienheim, 2003, pp. 173–179.

19 H. Qi and T. Hegmann, *J. Mater. Chem*., 2006, **16**, 4197.

20 T. Hegmann, H. Qi and V. M. Marx, *J. of Inorg. and Org. Pol. and Mat*., 2007, **17**, 483.

21 H. Qi, B. Kinkead and T. Hegmann, *Adv. Funct. Mater*., 2008, **18**, 212–221.

22 H. Qi and T. Hegmann, *Appl. Mat. & Interf*., 2009, **1**, 1731.

23 L. Cseh and G. H. Mehl, *J. Am. Chem. Soc*., 2006, **128**, 13376–13377.

24 L. Cseh and G. H. Mehl, *J. Mater. Chem*., 2007, **17**, 311–315.

25 V. M. Marx, H. Girgis, P. A. Heiney and T. Hegmann, *J. Mater. Chem*., 2008, **18**, 2983–2994.

26 X. Zeng, F. Liu, A. G. Fowler, G. Ungar, L. Cseh, G. H. Mehl and J. E. Macdonald, *Adv. Mater*., 2009, **21**, 1746–1750.

27 V. A. Mallia, P. K. Vemula, G. John, A. Kumar and P. M. Ajayan, *Angew. Chem. Int. Ed*., 2007, **46**, 3269–3274.

28 H. Yoshida, Y. Tanaka, K. Kawamoto, H. Kubo, T. Tsuda, A. Fujii, S. Kuwabata, H. Kikuchi and M. Ozaki, *Appl. Phys. Express*, 2009, **2**, 121501.

29 M. Ravnik, G. P. Alexander, J. Yeomans and S. Zumer, *Faraday Discuss.*, 2010, **144**, 159–169.

30 E. Karatairi, B. Rožič, Z. Kutnjak, V. Tzitzios, G. Nounesis, G. Cordoyiannis, J. Thoen, C. Glorieux and S. Kralj, *Phys. Rev. E*, 2010, **81**, 041703.

31 M. Ravnik, G. P. Alexander, J. M. Yeomans and S. Zumer, *Proc. Natl. Acad. Sci. USA*, 2011, **108**, 5188-5192.

32 M. Mitov, C. Portet, C. Bourgerette and E. Snoeck, *Nature Materials*, 2002, **1**, 229–231.

33 M. Mitov, C. Bourgerette and F. de Guerville, *J. Phys. Cond. Matt.*, 2004, **16**, S1981–S1988.

34 M. Mitov, C. Bourgerette and F. de Guerville, in *Nanofabrication Technologies*, Book Series: Proc. SPIE, 2003, **5220**, 20–27.

35 M. Mitov, F. de Guerville and C. Bourgerette, *Mol. Cryst. Liq. Cryst.*, 2005, **435**, 673–679.

36 T. J. Bunning and F.-H. Kreuzer, *Trends in Polym. Sci.*, 1995, **3**, 318–323.

37 F.-H. Kreuzer, N. Häberle, H. Leigeber, R. Maurer, J. Stohrer and J. Weis, in *Organosilicon Chemistry III*, ed. N. Auner and J. Weiss, 1997, Wiley-VCH, Weinheim, pp. 566–586.

38 H.-J. Eberle, A. Miller and F.-H. Kreuzer, *Liq. Cryst*., 1989, **5**, 907–916.

39 M. L. Tsai, S. H. Chen and S. D. Jacobs, *Appl. Phys. Lett.*, 1989, **54**, 2395.

40 J.-M. Gilli, M. Kamayé and P. Sixou, *J. Phys*., 1989, **50**, 2911–2918.

41 J.-M. Gilli, M. Kamayé and P. Sixou, *Mol. Cryst. Liq. Cryst*., 1991, **199**, 79–86.

42 U. Singh and C. Hunte, *Mol. Cryst. Liq. Cryst*., 2001, **366**, 247–254.

43 S. Etienne, L. David, M. Mitov, P. Sixou and K. L. Ngai, *Macromolecules*, 1995, **28**, 5758–5764.

44 E. M. Korenic, S. D. Jacobs, S. Faris and L. Li, *Mol. Cryst. Liq. Cryst*., 1998, **317**, 221–235.

45 M. Mitov, A. Boudet and P. Sopena, *Eur. Phys. J. B*, 1999, **8**, 327–330.

46 C. Binet, M. Mitov and A. Boudet, *Mol. Cryst. Liq. Cryst.*, 2000, **339**, 111–123.

47 M. Mitov, C. Binet, A. Boudet and C. Bourgerette, *Mol. Cryst. Liq. Cryst.*, 2001, **358**, 209–223.

48 D. C. Zografopoulos, E. E. Kriezis, M. Mitov and C. Binet, *Phys. Rev. E*, 2006, **73**, 061701.

49 M. Belalia, M. Mitov, C. Bourgerette, A. Krallafa, M. Belhakem and D. Bormann, *Phys. Rev. E*, 2006, **74**, 051704.

50 E. M. Korenic, S. D. Jacobs, S. M. Faris and L. Li, *Color Reas. & Appl*., 1998, **23**, 210–220.

51 E. M. Korenic, S. D. Jacobs, S. Faris and L. Li, *Mol. Cryst. Liq. Cryst*., 1998, **317**, 197–219.

52 A. Trajkovska, R. Varshneya, T. Z. Kosc, K. L. Marshall and S. D. Jacobs, Adv. Funct. Mater., 2005, 15, 217–222

53 P. V. Shibaev, P. Rivera, D. Teter, S. Marsico, M. Sanzari, V. Ramakrishnan and E. Hanelt, *Optics Express*, 2008, **16**, 2965–2970.

54 P. V. Shibaev, in *Liquid Crystal Microlasers*, ed. L. M Blinov and R. Bartolino, Transworld Research Network, Kerala, 2010, pp. 127–140.

55 G. Agez, R. Bitar and M. Mitov, *Soft Matter*, 2011, **7**, 2841–2847.

56 K. H. Yang, *J. Appl. Phys*., 1988, **64**, 4780–4781.

57 Y. Bouligand, *J. Phys.*, 1972, **33**, 715–736.

58 A. Saupe, *Mol. Cryst. Liq. Cryst.*, 1973, **21**, 211–238.

59 J. Rault, *C. R. Acad. Sc. Paris*, 1971, **272**, 1275–1276.

60 P. E. Cladis, M. Kléman and P. Pieranski, *C. R. Acad. Sc. Paris*, 1971, **273**, 275–277.

61 The limits of the thickness ranges are indicative values; the pattern transition does not occur abruptly at a critical thickness.

62 T. J. Bunning, D. L. Vezie, P. F. Lloyd, P. D. Haaland, E. L. Thomas and W. W. Adams, *Liq. Cryst*., 1994, **16**, 769–781.

63 J. Pierron, A. Boudet, P. Sopena, M. Mitov and P. Sixou, *Liq. Cryst*., 1995, **19**, 257–267.

64 A. Boudet, C. Binet, M. Mitov, C. Bourgerette and E. Boucher, *Eur. Phys. J. E*, 2000, **2**, 247–253.

65 J. Pierron, V. Tournier-Lasserve, P. Sopéna, A. Boudet, P . Sixou and M. Mitov, *J. Phys. II France*, 1995, **5**, 1635–1647.

66 A. Boudet, M. Mitov, C. Bourgerette, T. Ondarçuhu and R. Coratger, *Ultramicroscopy*, 2001, **88**, 219–229.

67 V. A. Belyakov and V. E. Dmitrienko, *Sov. Sci. Rev. A Phys.*, 1989, **13**, 1–212.

68 P.-G. de Gennes and J. Prost, *The Physics of Liquid Crystals*, 1993, Oxford University Press, Oxford, pp. 264–268.

69 M. Mitov, *Les Cristaux Liquides*, Presses Universitaires de France, Paris, 2000, pp. 44–49.

70 J. C. Payne and E. L. Thomas, *Adv. Funct. Mat*., 2007, **17**, 2717–2721.